AGU PUBLICATIONS

Space Weather

RESEARCH ARTICLE
10.1002/2017SW001768

Space Weather Influence on Electromagnetic Geosynchronous Debris Perturbations Using Statistical Fluxes

Joseph Hughes[1] and **Hanspeter Schaub**[1]

[1] Department of Aerospace Engineering, University of Colorado Boulder, Boulder, CO, USA

Key Points:
- This paper develops a charging model for aluminum using statistical fluxes at $K_P = 2-$ and $K_P = 8$
- This paper investigates the effect of electromagnetic perturbations and attitude uncertainty for high area-to-mass ratio debris
- This paper shows that eddy torques are roughly equivalent to 1 degree of attitude uncertainty for the object studied

Correspondence to:
J. Hughes,
joseph.hughes@colorado.edu

Citation:
Hughes, J., & Schaub, H. (2018). Space weather influence on electromagnetic geosynchronous debris perturbations using statistical fluxes. *Space Weather*, *16*, 391–405. https://doi.org/10.1002/2017SW001768

Received 15 NOV 2017
Accepted 16 FEB 2018
Accepted article online 22 FEB 2018
Published online 16 APR 2018

Abstract Due to the space plasma and the Sun, spacecraft at geosynchronous Earth orbit can charge naturally negative tens of kV. This charging can cause arcing which can damage spacecraft electronics and solar panels. A charged spacecraft will also experience a perturbative force and torque due to Earth's electric and magnetic fields. These electromagnetic perturbations have recently been postulated to cause significant orbital changes for lightweight debris objects. This paper investigates the effects of electromagnetic perturbations by using a charging model that uses measured flux distributions to better simulate natural charging and includes the convection electric field. This is done for a calm space weather case of $KP = 2-$, a stormy case where $KP = 8$, and a worst possible case where the voltage is held at -30 kV the entire time. It is found that neglecting electromagnetic effects on lightweight Mylar debris can lead to 100 km displacements after only a one orbit, and the covariance associated with such objects must be increased during periods of high charging.

Plain Language Summary This paper investigates how important often-neglected electromagnetic forces and torques are to predict the motion of space objects. It is found that for certain objects they can make a large difference.

1. Introduction

The dominant effects of space weather on satellite orbits are density variations which affect satellite drag in low Earth orbit at altitudes between 300 and 1,500 km, and spacecraft charging at geosynchronous Earth orbits (GEO). Spacecraft charging can lead to arcing, which can damage solar panels and damage spacecraft electronics. The SCATHA mission showed that charging naturally to tens of kV in Earth's shadow is possible (Fennell et al., 1983; Mullen et al., 1986). If the spacecraft is not continuously conducing, different parts of the spacecraft can charge to different levels and arc, which can damage spacecraft electronics (Ferguson et al., 2017). However, recent work by Früh et al. (2014), Hughes and Schaub (2016, 2017a), and Paul and Früh (2017) suggests that spacecraft charging can affect the orbits of lightweight debris objects as well. This has major implications for those wishing to track debris objects in GEO to prevent collisions. This is especially important as lightweight debris from the "graveyard" GEO orbit can easily drift back into the operational GEO orbit and threaten valuable space assets. Additionally, understanding this possible new link between space weather and GEO orbital perturbations has the possibility to benefit both fields.

Spacecraft are subject to a number of small forces that perturb their orbits from the closed-form conic section solution to the two body problem. At low altitudes, Earth's nonspherical gravity and drag strongly perturb certain orbits. Further out in GEO, all objects are perturbed by lunar and solar gravity, and some high area-to-mass (HAMR) objects are strongly perturbed by solar radiation pressure (SRP) (Schildknecht et al., 2004). However, not all orbits are explained using just the above perturbations; Wiesel (2016) reports some near-GEO debris objects which appear to accelerate *toward* the Sun during the propagation interval, which is impossible with only SRP disturbances. The primary source of this discrepancy is postulated to be that these objects are interacting with Earth's magnetic field.

Some of these unknown objects are thought to be torn off pieces of multilayer insulation (MLI) as discussed by Schildknecht et al. (2008). Samples returned from the Hubble Space Telescope showed cracks in areas of constrained loading, and Dever et al. (1998) discuss a tendency of MLI to curl up when peeling off. Fennell et al. (1983) discuss how GEO spacecraft could charge to very high potentials during geomagnetic storms.

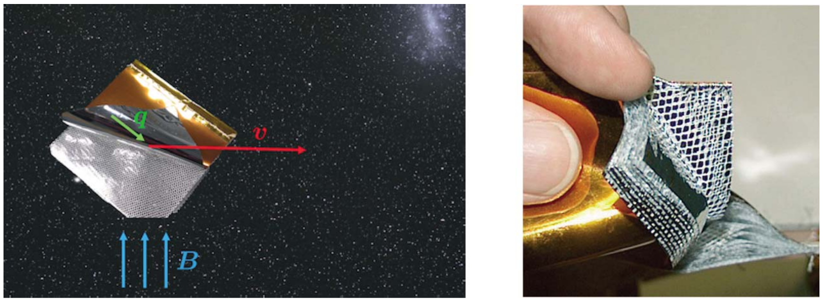

(a) Electromagnetic perturbations acting on charged MLI

(b) Multi Layer Insulation with non-conducting mesh shown

Figure 1. Multilayer insulation (MLI) with electrostatic perturbations.

This charging causes a translational Lorentz force and may cause a significant electrostatic torque depending on the relative distance between the center of charge and center of mass. Additionally, if the object is rotating relative to an external magnetic field, it experiences an eddy current torque.

Früh et al. (2014) were the first to publish results modeling the electrostatic charging effects on HAMR objects. This initial work adds the Lorentz force and eddy torque to the more standard list of perturbations for a HAMR plate. Including these two new effects changes the orbit by nearly a tenth of a degree in inclination and 0.002 in eccentricity after only 12 h. Paul and Früh (2017) model a sphere for which torques are not included and found much less dramatic results. Hughes and Schaub (2017a) consider a rigid plate similar to Früh et al. (2014) but included electrostatic torques and found that charging affects orbits primarily through electromagnetic torques rotating the object so that it experiences different SRP forces.

This work builds off the dynamical insights gained from Paul and Früh (2017) and Hughes and Schaub (2017a) by adding a more realistic charging model. In particular, the orbit averaged GEO space weather variations are taken into account as well as the convection E field. Finally, a statistical analysis over initial attitude is performed to study the relative sensitivity of the electrostatic and eddy current disturbance relative to other orbital perturbations. In Hughes and Schaub (2017a), a worst-case charging environment of -30 kV is assumed for the entire orbit. In this work, measured flux distributions at every local time are used to compute the equilibrium charging level at that point in the orbit. Additionally, this work considers a more complex debris object than a square plate or sphere: a thicker piece of MLI consisting of two separate pieces of aluminized mylar electrically separated by a piece of nonconducting tule. MLI normally has more than 40 layers of metalized sheets and mesh as shown in Figure 1, but in this work only the three layer system is considered. This two conductor system has the interesting property that one conductor is in the sunlight at all times and one is shaded. The presence of sunlight is very important for spacecraft charging with most objects charging a few volts positive in the sunlight and very negative in shade.

The statistical analysis looks at the relative significance of including electromagnetic perturbations and uncertainty in the initial attitude. In contrast, Hughes and Schaub (2017a) vary the initial attitude, but no analysis over how the size of the initial attitude change relates to the propagation model used is made. This work is done by first reviewing the space environment at GEO in both calm ($K_P = 2-$) and stormy ($K_P = 8$) conditions and then evaluating the spacecraft charging considering the statistical flux distributions to compute the currents. Next, methods for computing the new electromagnetic perturbations are reviewed with special emphasis on the debris object in question. The debris object is then propagated in a full attitude-dependent, 6 degrees of freedom simulator to investigate the change in dynamics from including or neglecting electromagnetic perturbations. The goal of this paper is a detailed discussion of how space weather conditions can change lightweight GEO debris orbits.

2. The Space Environment

The geosynchronous orbit regime lies near the boundary between the inner and outer magnetosphere at a radius of ~6.6 Earth radii or 42,164 km. The motion of the plasma in the inner magnetosphere is governed

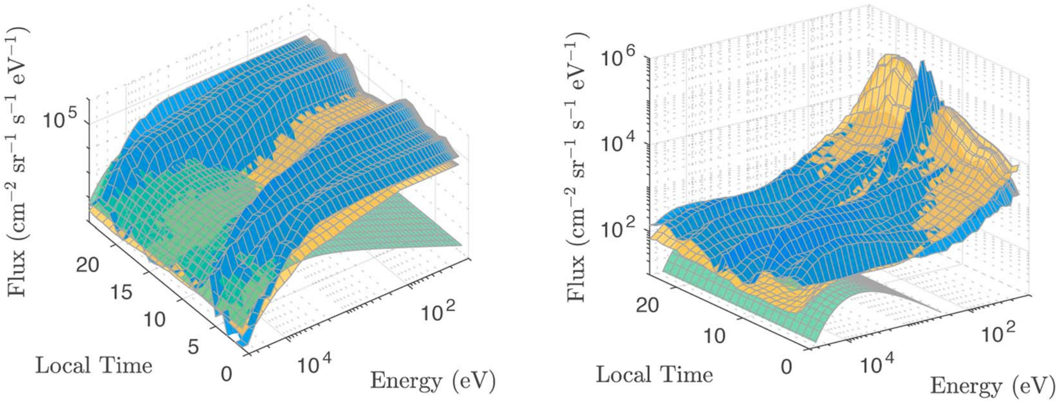

(a) Electron Fluxes (b) Ion Flux

Figure 2. Ion fluxes at geosynchronous Earth orbit for $K_P = 2-$ (yellow), $K_P = 8$ (blue), and a Maxwellian fit (green).

mainly by curvature and gradient drift, while the outer magnetosphere transitions to the global magnetospheric convection cycle. For the purposes of spacecraft charging, the electron and ion populations are often approximated as single or double Maxwellian distributions. While Maxwellian distributions are very easy to use, they do not match measured data well. Denton et al. (2015) present an empirical model that uses 82 satellite years of observed electron and ion flux data. Both populations are measured by magnetospheric plasma analyzers on board multiple Los Alamos National Labs satellites. The magnetospheric plasma analyzers are capable of measuring the flux between 1 eV and 40 keV in three spatial dimensions every 86 s. All of these data over the 82 satellite years of data are tagged with local time (LT), K_P index, and solar wind electric field (vB_z). Denton's model allows users to specify three inputs (energy, LT, and K_P or vB_z) and outputs the mean, median, and percentile flux values. K_P is a measure of the severity of geomagnetic storms and varies from 1 to 9 with three steps within each number, so 3+ is worse than 3, which is worse than 3−. This work considers a calm case where $K_P = 2-$ and a severe storm with $K_P = 8$.

The statistical mean electron fluxes for GEO are shown in Figure 2, with the yellow sheet indicating $K_P = 2-$, the blue sheet for $K_P = 8$, and the green sheet is a double Maxwellian fit from 4 September 1997 with n_e = 3E5, 2E5 cm^{-3}, T_e = 4, 7 keV, and n_i = 3E5, 2E5 cm^{-3}, T_i = 4, 7 keV (Davis et al., 2011). The measured flux at low energies is a combination of the natural space environment and the secondary and photoelectrons generated by the spacecraft itself. To avoid double-counting these electrons, the flux at all energies below 100 eV are reassigned to the flux at 100 eV which is why the surfaces are flat with respect to energy below 100 eV in Figure 2.

The storm conditions differ in many ways from the quiet condition—the flux is higher nearly everywhere, except for local times near 12:00, which corresponds to the Sun line. The shape of the flux in energy space is also different with more flux at higher energies during a storm. Both of these measurements differ significantly from the Maxwellian fit. In the low-energy region, the Maxwellian grossly underestimates the flux by 5 orders of magnitude. In the high-energy region the Maxwellian overestimates the flux, but not by nearly as large of a factor.

The statistical mean ion fluxes for GEO are shown in Figure 2, with the yellow sheet indicating $K_P = 2-$, the blue sheet for $K_P = 8$, and the green sheet is the same Maxwellian fit but for ions. Once again, the storm time flux is greater than the quiet time flux, but unlike the electrons, this trend is more dramatic at high energy. At low-energy the storm flux is actually lower. In LT, the trend seen in the electrons is reversed—there are more ions clustered near 12:00 during a storm. The Maxwellian fit is radically different from the measured data, does predict a similar order of magnitude in the 10 keV region.

3. Spacecraft Charging

A space object is subject to many currents from the space plasma and the Sun. The currents considered here are the thermal electron and ion currents (I_e, I_i) from the plasma, secondary electron emission (SEE) from both electrons and ions (I_{SEE_e}, I_{SEE_i}), electron backscattering (I_b), and the photoelectric current (I_ph) if the object is sunlit. The sign convention is for the currents to the spacecraft—so all currents except for the electron thermal current are positive. The object is in equilibrium when the net current to it is zero:

$$I_e(\phi) + I_i(\phi) + I_{\mathrm{SEE}_e}(\phi) + I_{\mathrm{SEE}_i}(\phi) + I_b(\phi) + I_{\mathrm{ph}}(\phi) = 0 \tag{1}$$

All these currents are functions of the object's voltage ϕ as well as many other parameters. Since the charging times for the objects considered here are so short, the object is always considered to be in equilibrium with its environment. Therefore, for each set of environmental conditions, the appropriate voltage can be prescribed by finding the voltage that drives the net current to zero. Each of the currents are discussed in detail in the following subsections.

3.1. Electron and Ion Currents

Electrons and ions impact the spacecraft, electrons causing a negative current and ions stealing an electron and causing a positive current. The magnitude of these currents is dependent on the amount of ions and electrons in the environment as well as the voltage of the spacecraft. For a flux distribution over energy $F(E)$, the current is

$$I(\phi) = q_0 A 4\pi \int_L^\infty \left(\frac{E}{E \pm \phi}\right) F(E \pm \phi) \mathrm{d}E \tag{2}$$

where q_0 is the particle charge, A is the area exposed to the plasma, and ϕ once again is the spacecraft potential. The lower bound of the integral L is 0 for the repelled particle and $|\phi|$ for the attracted particle. Ions take the upper sign and electrons take the lower. If a Maxwellian distribution is used, the integral can be solved analytically and the current is given by

$$I(\phi) = \begin{cases} I_0 \left(1 + \frac{q_0 \phi}{kT}\right) & \text{Attracted} \\ I_0 e^{q_0 \phi / kT} & \text{Repulsed} \end{cases} \tag{3}$$

where kT is the thermal energy of the plasma, q_0 is the fundamental charge, and I_0 is the current when the spacecraft is at 0 V, found from the parameters in the Maxwellian distribution. The dominant trends are linear attraction with a characteristic voltage equal to the temperature of the Maxwellian, and exponentially decreasing repulsed current.

In this analysis, measured flux distributions are used and these integrals are done numerically using an adaptive quadrature integration program that uses linear interpolation on the flux data. The flux data are logarithmically spaced in 40 increments for $K_P = 2$ and 50 increments for $K_P = 8$ as shown in Figures 2a and 2b. The lower bound for the attracted particle is $|\phi| + 0.1$ V to avoid a singularity, and since data for $F(E)$ only exists up to 40 keV for the distributions used, the upper bound is taken as $40,000 \text{ V} + \phi$.

3.2. Secondary Electron Emission and Backscattering Current

3.2.1. General Secondary Electron Emission

When an electron or ion impacts a material, it deposits much of its energy in the first few nanometers of the material. Some of this energy goes into freeing electrons near the surface which can be ejected. This phenomenon is referred to as SEE and can significantly reduce the net electron thermal current and amplify the ion thermal current. Additionally, there is a chance that an electron bounces off the material rather than sticking. This phenomena is called "backscatter." The probability that an electron backscatters is given by η, the expected number of secondary electrons generated is typically given by δ, and the total yield as Y. Since the total yield is a function of energy, it must be integrated over the distribution to find the current

$$I(\phi) = q_0 A 4\pi \int_L^\infty Y(E) \left(\frac{E}{E \pm \phi}\right) F(E \pm \phi) \mathrm{d}E \tag{4}$$

Typically, rather than calculating the actual current the mean yield $< Y >$ is used which is the effective yield for a particular distribution.

$$< Y > = \frac{I_Y}{I} = \frac{\int_L^\infty Y(E) \left(\frac{E}{E \pm \phi}\right) F(E \pm \phi) \mathrm{d}E}{\int_L^\infty \left(\frac{E}{E \pm \phi}\right) F(E \pm \phi) \mathrm{d}E} \tag{5}$$

Since $< Y >$ is constant for the repulsed particle if the distribution is Maxwellian and has very little variation for the attracted particle, $< Y >$ is often treated as a constant. In this analysis, it is treated as a function of the distribution (which is a function of LT) and the spacecraft voltage ϕ which shifts the distribution. Once again,

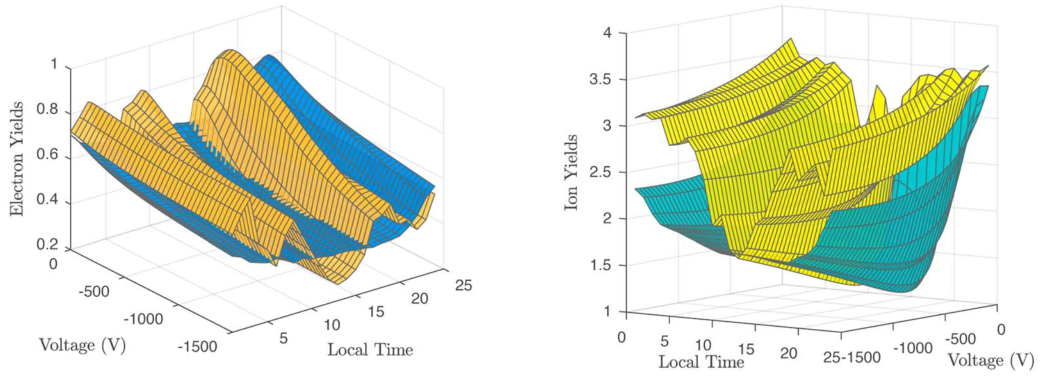

(a) Electron-Induced yields for $K_P = 8$ (orange), $K_P = 2$ (blue) as a function of Local Time and voltage

(b) Ion-Induced yields for $K_P = 2$ (teal), $K_P = 8$ (yellow) as a function of Local Time and voltage

Figure 3. Electron and Ion yields for aluminum.

this integral is done numerically using an adaptive quadrature integration program. The integration limits are the same as in the preceding subsection. The SEE function δ for both ion and electron impact as well as the backscattering function η are discussed next.

3.2.2. Electron-Induced SEE

The electron-induced SEE yield is typically low at low landing energies, then it rises to a large value, often larger than 1, for intermediate energies around a few hundred eV, and then falls back to a small yield for keV energies. If the maximum yield is larger than 1, there is an incident energy region where incident electrons can cause a net positive current. In this work, the "universal curve" of Lin and Joy (2005) is used:

$$\delta(E) = \delta_M 1.28 \left(\frac{E}{E_M}\right)^{-0.67} \left(1 - \exp(-1.614(E/E_M)^{1.67})\right) \tag{6}$$

where δ_M is the max yield and E_M is the energy at which it occurs. For aluminum, the parameters $\delta_M = 0.97$ and $E_M = 400$ eV are used.

3.2.3. Electron Backscattering

Backscattering occurs when an electron is reflected from the spacecraft rather than absorbed. This analysis uses the model for energy-dependent backscattering provided in Davis and Mandell (2011):

$$\eta(E) = \left(\frac{H(1-E)H(E-0.05)\log\left(\frac{E}{0.05}\right)}{\log(20)} + H(E-1)\right) \times \left(\frac{e^{-E/5}}{10} + 1 - (2/e)^{0.037Z}\right) \tag{7}$$

where E is the landing energy in keV, $H(x)$ is the Heaviside step function, and Z is the atomic number of the material (aluminum in this analysis). The formulas above can be added to produce the total yield $Y(E) = \eta(E) + \delta(E)$ for normally incident monoenergitic electrons.

3.2.4. Ion-Induced SEE

Ions may also cause SEE, and for many materials the number of secondaries caused by ions is much larger than that caused by electrons. However, since the ion current is usually much smaller than the electron current, ion-induced SEE is neglected in many cases. In this analysis the two parameter Nascap-2k model Davis and Mandell (2011) is used

$$\delta(E) = \frac{\beta E^{1/2}}{1 + E/E_M} \tag{8}$$

where E is the energy in keV and for aluminum $\beta = 1.36$ and $E_M = 40$ are fitting parameters.

3.2.5. Mean Yields

The above formulas for SEE and backscattering are inserted into equation (5) to calculate $< Y >$ for electrons and ions as a function of both space weather and local time for both space weather conditions. This is shown in Figures 3a and 3b.

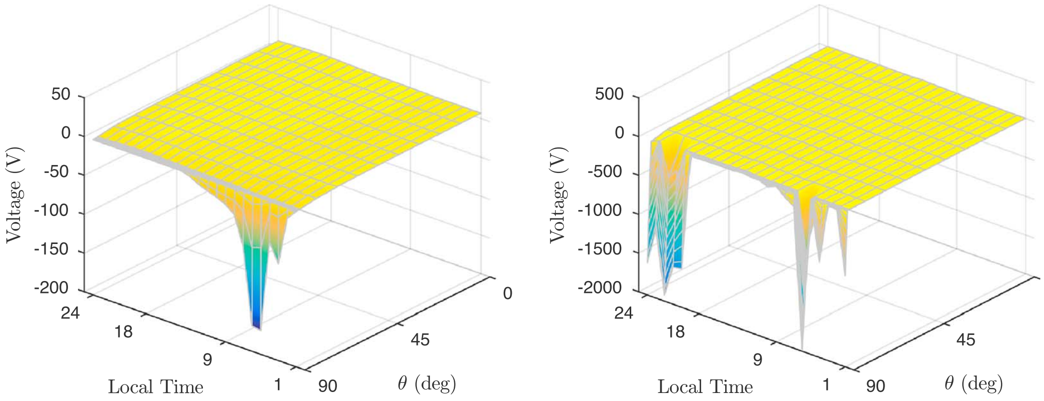

(a) Equilibrium voltage at $K_P = 2-$ (b) Equilibrium voltage at $K_P = 8$

Figure 4. Equilibrium voltage as a function of Sun incidence angle and local time.

Figure 3a shows the electron yields for stormy and calm space weather conditions. The effective yield is zero for a positive craft since although secondaries are generated, they are recollected by the craft. The yield is always less than 1, but it gets very close for low voltages where there are still a lot of low-energy particles. The dependence on local time is much more dramatic during the storm, which matches the higher dependence for the flux. At local noon, the storm yields are lowest, which matches the depleted low-energy section of the flux. Although the local time dependence for the flux is low in the morning and afternoon/night sectors in the flux, the yields have high dependence there.

Figure 3b shows the ion yields, which are much higher than the electron yields, although since the incident ion flues are much lower, this current is smaller than the electron-induced yields. There is a huge dip around local noon for the storm case, just as with the electron yields. Since the peak for ion-induced SEE is at much higher energies in the keV range, this matches the increase in low-energy ions and decrease in high-energy ions observed around local noon.

3.3. Photoelectric Current

Energy from the Sun can energize electrons in the first few nanometers of the spacecraft so that they leave the surface. The fraction that have enough energy to escape the potential well of the spacecraft causes a net positive current given by Lai (2011)

$$I_p = \begin{cases} j_{\mathrm{ph}} A \cos(\theta) e^{-q\phi/k_B T_{\mathrm{ph}}} & \phi > 0 \\ j_{\mathrm{ph}} A \cos(\theta) & \phi \le 0 \end{cases} \tag{9}$$

where j_{ph} is the photoelectron flux, A is the area, θ is the angle of incidence, and $k_B T_{\mathrm{ph}}$ is the thermal energy of the ejected photoelectrons. For aluminum, $k_B T_{\mathrm{ph}} = 2$ eV and $j_{\mathrm{ph}} = 40$ μA/m^2. For a negative spacecraft this current is constant, and for a positively charged spacecraft it quickly vanishes.

3.4. Equilibrium Voltage

Equation (1) can be solved at each local time and each Sun facing angle θ to provide a lookup table to interpolate and determine the voltage of both plates at any point in the orbit. Assuming the voltage to always be at the equilibrium value is justified since the charging time is very short compared to the orbit time.

Figure 4a shows the equilibrium voltage for aluminum as a function of local time and Sun incidence angle. An angle of 90 or greater indicates that the object is shaded and has no photoelectric current. Most of the charging happens in the absence of sunlight, and in the early morning sector when LT is between 0 and 6. This matches intuition as high-energy electrons cluster in that region due to their drifts. The most negative voltage occurs when the spacecraft is entirely shaded and at a local time of 5 and is −170 V. For $\theta < 88°$, the voltage varies between 5 and 10 V positive as expected for a sunlit object in calm space weather.

Figure 4b shows the equilibrium voltage in the same format as Figure 4a but for the stormy condition of $K_P = 8$. Again, most of the charging occurs for shaded or almost shaded angles, although the minimum angle moves down by a few tenths of a degree. The charging occurs in the early morning sector and also very dramatically in the late night sector where LT is between 20 and 24. The charge levels are much lower here as well, dropping to −1.9 kV at LT = 6 and −1.8 kV at LT = 22. Additionally, the voltage stays below −1 kV for the entire sector between LT = 20 and 24. There is good intuition for the existence of high charging in the early morning sector due to the electron drift, but the strong charging in the late night sector is unexpected. Even at this high K_P index, there is still not enough flux in the high-energy region where the yield is low to cause very severe charging. Once again, the fully sunlit voltages range between 5 and 10 V positive. Each sheet is assigned the voltage corresponding to the LT, and its Sun angle θ since the plates are not electrically connected. This means that one plate is always shaded while the other is always sunlit.

These results for voltage must be taken with a grain of salt as they depend on a number of parameters. First, the photoemission for aluminum is chosen as the round number of 40 μA/m^2 to match that used by Nascap-2k. Second and most importantly, the model parameters for electron-induced SEE have a good amount of variability. The max yield used here of 0.97 and in Nascap-2k is reported as 2.0 by Lin and Joy (2005) and found experimentally to be near 2.5 by Balcon et al. (2012). Additionally, Balcon et. al. found that the SEE parameters had a strong dependence on the angle of incidence (an electron that has grazing incidence creates more secondaries since it deposits more energy close to the surface where the secondaries have a better chance or escaping). There is also dependance on the surface condition (smooth or rough) and the temperature of the sample. This work also only considers normally incident flux.

If a maximum yield of 2.0 is used, the voltages range from 0 to 17 V positive even in shade. This is because the net electron yield is greater than 1, and the instant the spacecraft starts to charge negative the SEE current turns on and pushes it back to positive since the secondary electrons can now escape the system. With these much less dramatic voltages, the resulting electrostatic perturbations are much more subdued.

4. Propagation Model

Consider a small piece of torn off MLI 50 cm by 50 cm like that shown in Figure 1. It is composed of just three layers: two layers of aluminized mylar 6.35 μm (1/4 mil) thick with a nonconducting piece of Dacron netting 0.16 mm thick in between. The total mass of this thin sheet is just 6.225 g, but its large surface area of 0.25 m^2 gives it an area to mass ratio of 40.16 m^2/kg. All MLI parameters are taken from Finckenor (1999). The center of mass is assumed to be offset from the center of pressure by [2.5, 2.5, 0] cm due to some wrinkling or other imperfection. The center of charge is assumed to be offset from the center of mass by [−2.5, −3.33, 0] cm. The inertia tensor is computed assuming constant density.

The primary force for macrosized objects in Earth orbit is the Earth's gravity. There are several small forces and torques which perturb the orbits of many small objects such as SRP, Earth's non–point mass gravity, and the gravitational pull of the Sun and Moon. This work includes three new electromagnetic perturbations—the Lorentz force, the Lorentz torque, and eddy current torques. All perturbations are listed in Table 1 with either the exact equation or a short description.

The zonal and tesseral harmonics of Earth's gravity are used up to fourth order. The torque is given by the gravity gradient. Point mass gravity is used for lunar and solar gravity.

4.1. Solar Radiation Pressure

The Absorbed and Specular and Diffuse (ASD) reflection model is used to model SRP. The magnitude of the SRP force is determined by the solar flux and the illuminated area. The direction is governed by the amount of light that is absorbed and reflected specularly and diffusely. The SRP force is given by Wie (2008)

$$\boldsymbol{F} = p_{\mathrm{SRP}} A \cos(\theta) \left[\rho_A \hat{\boldsymbol{s}} + 2\rho_s \cos(\theta) \hat{\boldsymbol{n}} + \rho_d \left(\hat{\boldsymbol{s}} + \frac{2}{3} \hat{\boldsymbol{n}} \right) \right] \tag{10}$$

where θ is the angle between the Sun-pointing line and the face normal, $\hat{\boldsymbol{s}}$ is the Sun-pointing vector, $\hat{\boldsymbol{n}}$ is normal to the plane, and $\rho_A, \rho_S,$ and ρ_D are the absorptive, specular, and diffuse coefficients, respectively, which must sum to unity. In this analysis, $\rho_A = 0.5$, $\rho_S = 0.2$, and $\rho_D = 0.3$.

4.2. Magnetic Field Models

Both the Lorentz force and torque as well as the eddy torque depend on the strength and direction of the magnetic field. There are many approximations for Earth's magnetic field. The first and simplest is the dipole approximation, next is the International Geomagnetic Reference Field model, and the third is the Tsyangenko model, which merges the International Geomagnetic Reference Field with the solar wind (Tsyganenko, 1989).

Table 1
Forces and Torques Acting on Space Debris

Perturbation	Force	Torque
Earth gravity	Spherical harmonics	$\boldsymbol{L} = \frac{3\mu}{R_c^5}\boldsymbol{R}_c \times [I]\boldsymbol{R}_c$
Lunar gravity	Point mass gravity	0
Solar gravity	Point mass gravity	0
SRP	ASD reflection	$\boldsymbol{L} = \boldsymbol{r}_{\text{sep}} \times \boldsymbol{F}_{\text{SRP}}$
Electromagnetic	$\boldsymbol{F} = Q\boldsymbol{A}$	$\boldsymbol{L} = \boldsymbol{q}_{\text{sep}} \times \boldsymbol{A}$
Eddy currents	0	$\boldsymbol{L} = ([M](\boldsymbol{\omega} \times \boldsymbol{B})) \times \boldsymbol{B}$

Note. SRP = solar radiation pressure.

There have been many versions and updates to the Tsyganenko model, but in this analysis the 2001 version is used with GEOPACK 2008 for coordinate transforms.

Since the magnetic field is position dependent, the model is run at each time step. The time is assumed to be 1 January 2000, midnight, for all runs. The space weather parameters used are the representative values that are used by the Community Coordinated Modeling Center on their single-run website.

4.3. Electric Field Models

The corotation and convection electric field both contribute to electric perturbations. The corotation field uses the Tsyganenko model discussed above for the magnetic field and the Volland-Stern (Stern, 1975; Volland, 1973) model for the convection E field as presented in Korth et al. (1999) which gives the voltage of a point in space as

$$V = -bL^{\gamma}\sin(\phi) \tag{11}$$

where b is a constant, γ is a constant, and $L = \frac{r/Re}{\sin^2(\theta)}$ is the magnetic L shell and ϕ is the magnetic local time referred to noon rather than midnight. The angle θ is the magnetic colatitude, which is measured downward from the magnetic north pole. In this work $\gamma = 2$, and $b = 45\ \text{V}/(1 - 0.159K_P + 0.0093\ K_P^2)^3$ is the overall strength as a function of K_P index (Chen, 1975). To find the colatitude, first transform into the geomagnetic frame (Bhavnani & Vancour, 1991) which has its third axis aligned with Earth's north magnetic pole and then take the inverse cosine of $r(3)/||r||$. To find ϕ, project the satellite and Sun position into the geomagnetic x-y plane and find the angle with respect the x axis for both and subtract them to find ϕ.

To find the E field, take the gradient in spherical coordinates $\boldsymbol{E} = -\nabla V$:

$$\boldsymbol{E} = -\nabla V = -\frac{\partial V}{\partial r}\hat{\boldsymbol{r}} - \frac{1}{r}\frac{\partial V}{\partial \theta}\hat{\boldsymbol{\theta}} - \frac{1}{r\sin(\theta)}\frac{\partial V}{\partial \phi}\hat{\boldsymbol{\phi}} \tag{12}$$

$$= \frac{V}{r}\left(-\gamma\hat{\boldsymbol{r}} + 2\gamma\cot(\theta)\hat{\boldsymbol{\theta}} - \csc(\theta)\cot(\phi)\hat{\boldsymbol{\phi}}\right) \tag{13}$$

where $\hat{\boldsymbol{r}}$ points outward, $\hat{\boldsymbol{\theta}}$ points southward (magnetically, not geographically), and $\hat{\boldsymbol{\phi}} = \hat{\boldsymbol{r}} \times \hat{\boldsymbol{\theta}}$.

This potential and the electric field are shown in geocentric solar magnetospheric coordinates below in Figure 5a for $K_P = 3$. In the figure, the length of the arrow represents the field strength with 1 axis unit representing 2 mV/m. The field is points from dawn to dusk as expected. At this low K_P level the average field strength is 0.434 mV/m, but if K_P increases to 8 it grows to 2.87 mV/m. Figure 5b shows both the Lorentz field

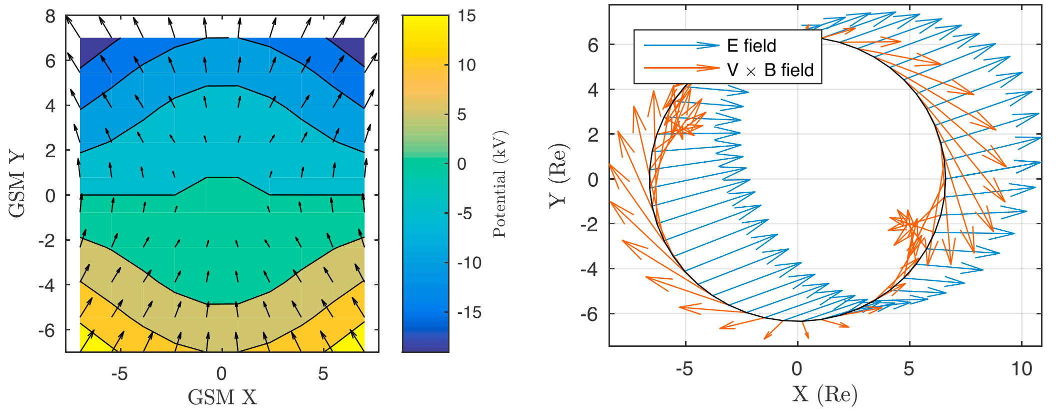

(a) Convection E field in GSM (b) E and V × B field for inclined GEO orbit

Figure 5. Convection E field and Lorentz field comparison for $K_P = 3$. GSM = geocentric solar magnetospheric; GEO = geosynchronous Earth orbit.

($\boldsymbol{v} \times \boldsymbol{B}$) and the convection E field in the Earth Centered Inertial x-y plane for a geosynchronous orbit inclined to 16°. The Sun is nearly directly below in this figure. Keep in mind that the $\boldsymbol{v}$ is the velocity relative to the magnetic field, which corotates with Earth and is not aligned with the orbit; thus, the Lorentz field is not perpendicular to the orbit. The length of the arrow once again represents the strength of the field at that point, with one axis unit corresponding to 0.1 mV/m for the convection E field or 0.01 mV/m for the Lorentz field.

The first thing to notice is that since the length of the vectors in Figure 5b are similar, the magnitude of the E field for this orbit is about 10 times stronger than the Lorentz field even at $K_P = 3$ (average magnitude for this orbit of 0.431 mV/m versus 0.036 mV/m); at $K_P = 8$ the difference is even greater since the average E field strength grows to 2.85 mV/m. In all prior work by Früh et al. (2014), Paul and Früh (2017), and Hughes and Schaub (2017a, 2016), the convection E field has been completely ignored in favor of the B field, but it is actually the stronger of the two. In different orbits, specifically one in which there is greater velocity relative to the magnetic field and is closer to Earth, the $\boldsymbol{v} \times \boldsymbol{B}$ field is stronger.

4.4. Electrostatic Force and Torque

4.4.1. General Development

The effective E field is $\boldsymbol{A} = \boldsymbol{E} + \boldsymbol{v} \times \boldsymbol{B}$ where $\boldsymbol{v}$ is the velocity relative to the magnetic field. The differential force on a differential charge moving through this field is (Griffiths, 1999)

$$\mathrm{d}\boldsymbol{F} = \mathrm{d}q\boldsymbol{A} \tag{14}$$

The torque about the center of mass on a body is defined as $\int_B \boldsymbol{r} \times \mathrm{d}\boldsymbol{F}$, where $\boldsymbol{r}$ points from the center of mass to the volume element. Using the differential force to find the net force and torque on a body gives

$$\boldsymbol{F} = \int_B \boldsymbol{A}\,\mathrm{d}q \tag{15}$$

$$\boldsymbol{L} = \int_B \boldsymbol{r} \times \boldsymbol{A}\,\mathrm{d}q \tag{16}$$

If a body is rotating, the velocity relative to the magnetic field varies over the body and $\boldsymbol{A}$ is dependent on the position. Assuming an orbit inclined at 16°, the relative velocity at GEO is ~1 km/s. If the body has a radius of 1 m and is rotating at 1°/s, the relative velocity from rotation is 10^{-5} times smaller than that from the orbit. In this analysis it is neglected and $\boldsymbol{v}$ is simply the translational orbital velocity.

Define the charge separation vector $\boldsymbol{q}$ and the total charge Q below to simplify the force and torque

$$Q = \int_B \mathrm{d}q \text{ and } \boldsymbol{q} = \int_B \boldsymbol{r}\mathrm{d}q \tag{17}$$

Using the definitions in equation (17) in the integrals in equations (15) and (16) gives the following results for force and torque:

$$\boldsymbol{F} = \boldsymbol{A}\,Q \qquad \boldsymbol{L} = -\boldsymbol{A} \times \boldsymbol{q} \tag{18}$$

4.4.2. Susceptibilities of AFM Parameters

This method for predicting force and torque is known as the Appropriate Fidelity Measures (AFM) method because of the measures (Q, $\boldsymbol{q}$) of the charge distribution it employs (Hughes & Schaub, 2017a). If the new variables Q and $\boldsymbol{q}$ were known at all times, equation (18) would be enough to predict force and torque; however, the charge distribution changes as the object rotates and changes voltage. This section quickly goes over how to predict the parameters Q and $\boldsymbol{q}$ using the plate voltages; a full explanation is given in Hughes and Schaub (2017b).

Using an elastance-based formulation, the voltage at every node $\boldsymbol{V}$ is given by

$$\boldsymbol{V} = [S]\boldsymbol{Q} \tag{19}$$

where $[S]$ is the elastance matrix and $\boldsymbol{Q}$ is the charge on each node. There are many ways to make $[S]$, including the Method of Moments (Gibson, 2007) and the Surface Multi-Sphere Method (Stevenson & Schaub, 2013). In this work Method of Moments is used, which gives the elements of $[S]$ for two parallel plates perpendicular to the z axis to be

$$S_{i,j} = \int_{-\Delta y/2}^{\Delta y/2} \int_{-\Delta x/2}^{\Delta x/2} \frac{\mathrm{d}x'\mathrm{d}y'}{\sqrt{(x_c + x')^2 + (y_c + y')^2 + z_c^2}} \tag{20}$$

where x_c, y_c are the center-to-center x and y displacements for the two area elements i and j and z_c is the displacement in the z direction. If $i = j$, x_c and y_c are both 0. To perform this integration, use the u substitutions $u = x_c + x$ and $v = y_c + y'$:

$$S_{i,j} = \int_{-\Delta y/2+y_c}^{\Delta y/2+y_c} \int_{-\Delta x/2+x_c}^{\Delta x/2+x_c} \frac{\mathrm{d}u\,\mathrm{d}v}{\sqrt{u^2+v^2+z_c^2}} \tag{21}$$

Denote the double antiderivative of this function by s, the elastance entry can be formed from the values of s on the four endpoints of dA:

$$S_{i,j} = s(u_+, v_+) + s(u_-, v_-) - s(u_+, v_-) - s(u_-, v_+) \tag{22}$$

where the ± subscripts determine the upper or lower limit of that variable. The double antiderivative s is given below:

$$\begin{aligned} s(u,v) = \int\int \frac{\mathrm{d}u\,\mathrm{d}v}{\sqrt{u^2+v^2+z_c^2}} &= v\log\left(\sqrt{u^2+v^2+z^2}+u\right) + u\log\left(\sqrt{u^2+v^2+z^2}+v\right) \\ &- z\tan^{-1}\left(\frac{uv}{z\sqrt{u^2+v^2+z^2}}\right) \quad + z_c\tan^{-1}\left(\frac{v}{z}\right) - v \end{aligned} \tag{23}$$

where log() is the natural logarithm (base e). Once $[S]$ is known, the charge on each node can be found by solving the linear system. A process for predicting the total charge Q and the dipole $\boldsymbol{q}$ on two nearby conductors is introduced in Hughes and Schaub (2017b); however, that work assumes that the distance between the conductors is larger than the conductors themselves. Thus, modifications must be made for this case where the plates are 50 cm in length, and only 160 μm apart. To derive the capacitance matrix for two plates, look at the system in block form:

$$\begin{bmatrix} \boldsymbol{Q}_1 \\ \boldsymbol{Q}_2 \end{bmatrix} = \begin{bmatrix} [C_{S_1}] & [C_M] \\ [C_M^T] & [C_{S_2}] \end{bmatrix} \begin{bmatrix} \boldsymbol{V}_1 \\ \boldsymbol{V}_2 \end{bmatrix} \tag{24}$$

since both plates are conductors, the voltage is constant across both of them: $\boldsymbol{V}_1 = V_1\mathcal{O}(n_1, 1)$ where n_1 is the number of elements used to model plate 1 and $\mathcal{O}(a, b)$ is a matrix consisting only of ones of size $[a, b]$. The total charges on each plate are given by $Q_1 = \sum_i^{n_1} \boldsymbol{Q}_1(i) = \mathcal{O}(1, n_1)\boldsymbol{Q}_1$; thus,

$$\begin{aligned} Q_1 &= \mathcal{O}(1,n_1)[C_{S_1}]\mathcal{O}(n_1,1)V_1 + \mathcal{O}(1,n_2)[C_M]\mathcal{O}(n_1,1)V_2 \\ &= C_{S_1}V_1 + C_M V_2 \end{aligned} \tag{25}$$

$$\begin{aligned} Q_2 &= \mathcal{O}(1,n_2)[C_M]\mathcal{O}(n_2,1)V_1 + \mathcal{O}(1,n_1)[C_{S_2}]\mathcal{O}(n_2,1)V_2 \\ &= C_M V_1 + C_{S_2}V_2 \end{aligned} \tag{26}$$

where the model for plate 2 contains n_2 elements. This shows that the elements of the capacitance matrix for two bodies are simply the sum of the elements of the blocks in the large capacitance matrix for every node. Because the two plates are exactly alike except for their relative positions, and because $[S]$ and $[C]$ are symmetric, $C_{S_1} = C_{S_2} = C_S$ and the mutual term C_M are the same. To find the susceptibilities of the dipoles, denote the positions of every node by

$$[R] = \begin{bmatrix} x_1 & x_2 & \dots & x_N \\ y_1 & y_2 & \dots & y_N \\ z_1 & z_2 & \dots & z_N \end{bmatrix} \tag{27}$$

for both plates R_1 and R_2. The dipole is given by

$$\boldsymbol{q} = \int_B \boldsymbol{r}\mathrm{d}q = \sum_{i=1}^{N} \boldsymbol{r}_i Q_i = [R]\boldsymbol{Q} \tag{28}$$

for a continuous charge and matrix formulation. Now combine with the form for $\boldsymbol{Q}$ from earlier

$$\begin{aligned} \boldsymbol{q}_1 &= \chi_{1,1}V_1 + \chi_{1,2}V_2 \\ \boldsymbol{q}_2 &= \chi_{2,1}V_1 + \chi_{2,2}V_2 \end{aligned} \tag{29}$$

Table 2
AFM Parameters for Predicting Lorentz Force and Torque

Parameter	Value
C_S	20.774 nF
C_M	−20.762 nF
$\chi_{1,1}$	[3.116, 0.692, 0.002] nFm
$\chi_{2,2}$	[3.116, 0.692, −0.002] nFm
$\chi_{1,2}$	[−3.114, −0.692, −0.002] nFm
$\chi_{2,1}$	[−3.114, −0.692, 0.002] nFm

where the χ parameters are given by

$$\chi_{1,1} = [R_1][C_{S_1}]\mathcal{O}(n_1, 1) \quad \chi_{1,2} = [R_1][C_M]\mathcal{O}(n_1, 1) \tag{30}$$

$$\chi_{1,2} = [R_2][C_M]\mathcal{O}(n_2, 1) \quad \chi_{2,2} = [R_2][C_{S_2}]\mathcal{O}(n_2, 1) \tag{31}$$

For the specific case of two 50 cm plates separated by a 160 μm space, both with their centers of mass displaced by [−2.5, −3.33, 0] cm, the electrostatic parameters are given in Table 2:

Since the two plates are held together, only the total dipole $\boldsymbol{q} = \boldsymbol{q}_1 + \boldsymbol{q}_2$ and total charge $Q = Q_1 + Q_2$ need to be considered. Finally, the equations for $\boldsymbol{q}$ and Q can be combined with equation (18) to yield the Lorentz force and torque from the voltages only

$$\begin{aligned} \boldsymbol{F} &= (C_S + C_M)(V_1 + V_2)\boldsymbol{A} \\ \boldsymbol{L} &= \left((\chi_{1,1} + \chi_{2,1})V_1 + (\chi_{1,2} + \chi_{2,2})V_2\right) \times \boldsymbol{A} \end{aligned} \tag{32}$$

Eddy current torque is included as well. When a conductor spins in a magnetic field, the mobile electrons move in loops because of induction. No net force is felt because the current path is closed, but an eddy current torque is felt. The formulation given in Ortiz Gomez and Walker (2015) is used.

5. Propagation Model Results

Now that all the forces and torques are detailed, the orbit of a HAMR object can be propagated. Once again the object is a 50 cm square piece of MLI with an area to mass ratio of 40.16 m^2/kg. This object is put in an initial orbit with $a = 42,164$ km, $e = 0.0001$, $i = 16°$, $\Omega = 0°$, $\omega = 242.3213°$, and $\nu = 85.05°$. The true anomaly ν is chosen so that the propagation begins at a local time of 4 h, which subjects the plate to the most dramatic charging. The initial angular rates are set to zero, and its initial attitude is aligned with the ECI frame ($\boldsymbol{\sigma} = [0, 0, 0]^T$) where $\boldsymbol{\sigma}$ is a Modified Rodriguez Parameter to describe the attitude (Schaub & Junkins, 2009). The orbit is propagated for 24 h with a 3 s time step using a RK4 integrator, and the resulting altitude departure and longitude are shown in Figure 6a.

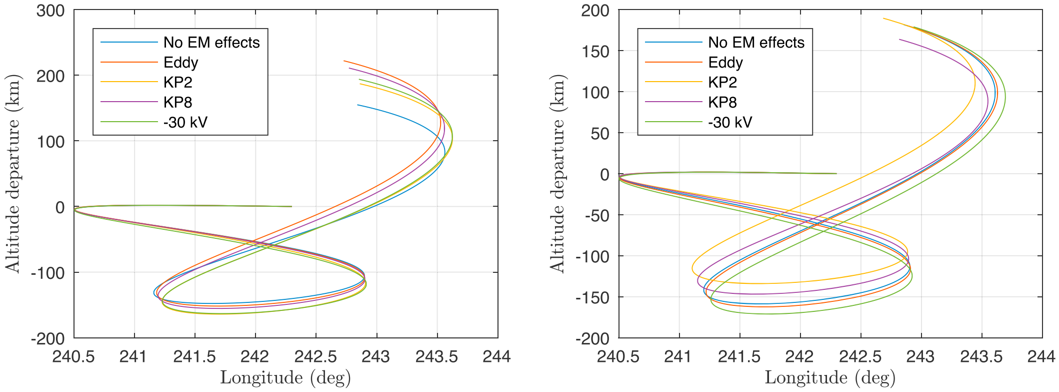

(a) Initial attitude $\boldsymbol{\sigma} = \begin{bmatrix}0 & 0 & 0\end{bmatrix}^T$ (b) Initial attitude $\boldsymbol{\sigma} = \begin{bmatrix}0.2 & 0 & 0\end{bmatrix}^T$

Figure 6. Latitude and altitude departure caused by neglecting perturbations.

In an unperturbed orbit, all the tracks would end in the same place as they began. However, they all are a few hundred kilometers higher in altitude and have traversed over more than 3° of longitude. For reference, the typical longitude spacing between satellites in GEO is ~0.5°. At the end of the propagation all five models predict different final positions. Using the model which only includes gravitational effects and SRP as a reference, including eddy torques gives a final position 109.48 km away. Including just electrostatics at $K_P = 2-$ and $K_P = 8$ gives final position differences of 35.98 and 77.32 km, respectively. Including just electrostatics with a worst-case constant voltage of −30 kV yields a final position difference of 40.23 km. These final positions are small numbers when compared to the orbit radius, but correspond to a few tenths of a degree which matters for telescope pointing.

Using these differences in final positions, it would seem that including eddy torques is the most important, since it leads to the largest position difference. Next would be electrostatics at $K_P = 8$, then a constant voltage of −30 kV, and then $K_P = 2$. This is quite surprising since the electric disturbances are strongest at −30 kV, not at $K_P = 8$. To further investigate which perturbations cause the largest differences in position, the same propagation is repeated, only changing the initial attitude to $\boldsymbol{\sigma} = [0.2, 0, 0]^T$. Again the altitude departure from the initial attitude and the longitude are shown in Figure 6b.

Here the object again follows a curving "figure 8" path and changes altitude by ~400 km and longitude by ~3°. However, the orbits are drastically different from those computed with the first attitude—for instance, the model that ignores all electromagnetic perturbations predicts a final altitude departure of more than 200 km with the first attitude, but less than 200 km with the second attitude. Additionally, the ordering of the relative impacts of the different perturbations is different. Choosing the model which ignores all electromagnetic effects as the reference, including eddy torques leads to a 14.58 km difference after 24 h, electrostatics at $K_P = 2-$ and 8 lead to differences of 130.38 and 33.85 km, and a constant voltage of −30 kV leads to a final position difference of 62.26 km. While eddy current torque is the most significant at the first attitude, it is the *least* at this attitude. $K_P = 2-$ and $K_P = 8$ switch places, and the constant −30 kV case is now less significant than electrostatics at $K_P = 2-$.

These simulation results illustrate that the initial attitude *and* the propagation model used both have a strong influence on the orbit. Because even the relative ordering of how significant different electromagnetic perturbations are gets reshuffled, it would appear that the initial attitude and the propagation model are coupled. This is not completely surprising, since the significant part of the electromagnetic perturbations is the torque, which changes the attitude and "steers" SRP (Hughes & Schaub, 2017a). Either a small torque (such as from electromagnetics) integrated over time or a different initial attitude results in a different attitude, which changes SRP, which changes the orbit. It is prudent to remember that this behavior is due in most part to the strongly attitude-dependent cross sectional area of this flat plate. A sphere with the same area to mass ratio is nowhere near as sensitive Paul and Früh (2017).

6. Statistical Analysis

The earlier section showed that the relative effect of different electromagnetic perturbations is not consistent for two different initial attitudes. This section looks at hundreds of initial attitudes to find which perturbations are the most significant. Additionally, the effect of including different electromagnetic perturbations is compared to initial uncertainty in attitude. To do this, the same 50 cm plate is propagated either with an initial attitude perturbation or including electromagnetic perturbations and then compared to a plate that had neither an initial attitude perturbation nor electromagnetic perturbations. This is shown schematically in Figure 7.

For all cases, a plate is put into orbit with the initial orbit elements of $a = 42,164$ km, $e = 0.0001$, $i = 16°$, $\Omega = 0°$, $\omega = 242.3213°$, and $\nu = 85.05°$. The true anomaly ν is chosen so that the propagation begins at a local time of 4 h, which subjects the plate to the most dramatic charging. A random initial attitude $\boldsymbol{\sigma}_i$ is generated from three uniformly distributed Euler angles. A plate with this attitude is propagated neglecting all electromagnetic effects for a period of time Δt, and its final position $\boldsymbol{r}_{\text{Ref}}$ is recorded. Next, a perturbation or initial attitude difference is added. For the attitude difference, a rotation of magnitude θ_j about a randomly selected axis $\hat{\boldsymbol{u}}$ where $\boldsymbol{\theta} = [0.0001°, 0.001°, 0.01°, 0.1°, 1°]$ using the principle rotation vector $\boldsymbol{\gamma} = \theta_j \hat{\boldsymbol{u}}$ and the final position $\boldsymbol{r}_{\text{Rotation}}$ after Δt is recorded. For the perturbations, the plate is not rotated but eddy torques, electrostatics at $K_P = 2-, K_P = 8$, or a worst-case constant voltage of −30 kV is included

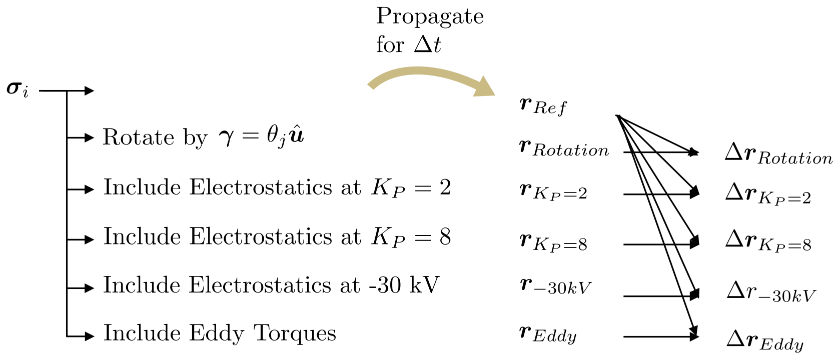

Figure 7. Scheme for investigating relative effect of electromagnetic disturbances with randomized initial attitude.

in the propagation and the final positions ($\boldsymbol{r}_{K_P=2}, \boldsymbol{r}_{K_P=8}, \boldsymbol{r}_{-30\text{kV}}, \boldsymbol{r}_{\text{Eddy}}$) are recorded. The electrostatic cases are run without eddy torques included. Finally, the difference in final positions between the reference $\boldsymbol{r}_{Ref}$ and the cases that include electromagnetic perturbations or have a different initial attitude is computed ($\Delta r_{\text{Rotation}}, \Delta r_{K_P=2}, \Delta r_{K_P=8}, \Delta r_{\text{Eddy}}$). This process is repeated 500 times varying the initial attitude $\boldsymbol{\sigma}_i$ each time recording the Δr every 15 min for 3 h in a master text file. The 10 cases, run for 3 h of simulation time, for 500 different initial attitudes gives 15,000 h of propagation time. The results of this propagation are shown in Figure 8.

The statistics for the effect of an initial attitude difference or including an electromagnetic perturbation are shown using violin plots. Violin plots are a way of looking at multiple histograms at once—the width of the bar represents how many counts are observed in the bin given by the position on the y axis. Violin plots can be thought of as a collection of histograms all rotated by 90°. The different ticks on the x axis represent different

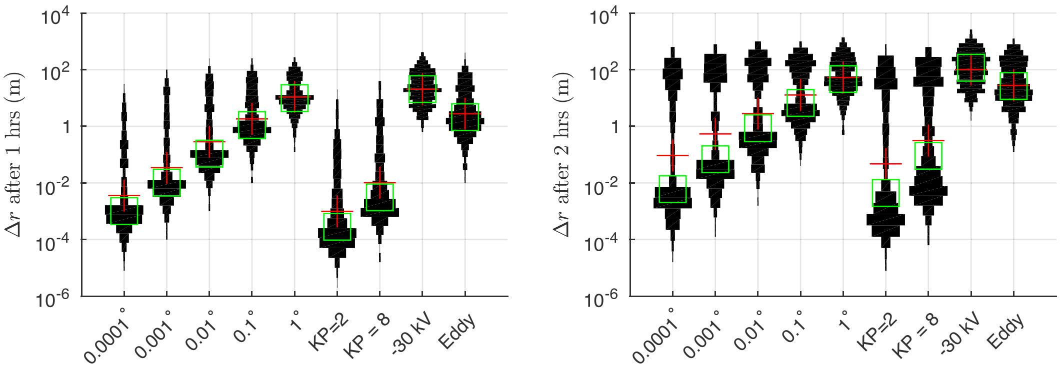

(a) After 1 hour (b) After 2 hours

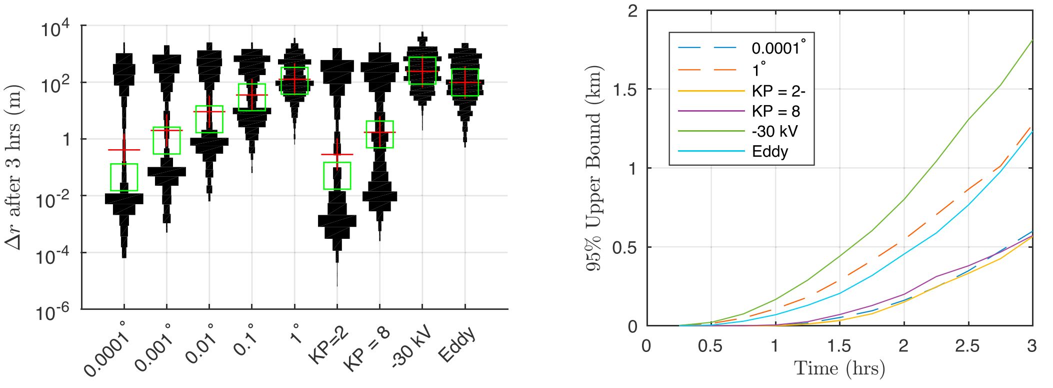

(c) After 3 hours (d) 95% covariance bounds

Figure 8. Results of propagation with varied initial attitude or perturbations.

cases. For example, consider the 0.0001° case after 3 h of propagation shown in Figure 8. The position difference from this initial attitude change is either less than 1 cm or in the hundreds of meters. Simply reporting the mean or median (shown in red and green, respectively) would lead one to believe that most of the initial attitudes lead to final position differences of ~1 m, when in reality almost none of them are.

At the 1 h mark (Figure 8a), including electrostatics with $K_P = 2-$ only causes position differences greater than a meter for very few initial attitudes; furthermore, it is *less* significant than a 0.0001° uncertainty in initial attitude, which is nearly impossible to get from a ground observation for a noncooperative object. If $K_P = 8$, a significant fraction of the initial attitudes lead to position difference of dozens of meters after only an hour, and including or neglecting electrostatics is equivalent to a little less than 0.001° uncertainty in initial attitude. If the worst case is observed and both sides of the plate are charged to −30 kV, almost all the initial attitudes lead to position differences greater than a meter after only an hour with a few exceeding 100 m. This is more significant than 1° of attitude uncertainty. Including eddy torques also causes a large spread and is comparable to 1° of uncertainty.

Moving to the 2 h mark of simulated orbit time, the distributions begin to look bimodal. One population of initial attitudes leads to large position differences greater than 10 meters, while the other leads to much smaller position differences. This may be because some attitudes lead to “runaway” differences while others lead to stable spins about the axis of maximum inertia which are much harder to perturb and change the attitude in a way that affects SRP (Hughes & Schaub, 2017a). It is still the case that electrostatics at $K_P = 2-$ are less significant than 0.0001° of attitude uncertainty, at $K_P = 8$ including electrostatics is roughly equivalent to 0.001° of attitude uncertainty, the worst case is more significant than 1° of uncertainty, and that including eddy torques is similar to 1° of uncertainty.

Moving finally to 3 h of simulated orbit time, now a very significant portion of all initial attitudes with all perturbations leads to position differences of more than 100 meters. The split between the runaway cases and the others is even more dramatic, causing many of the plots to take on a “dog bone” shape. Surprisingly, including eddy torques, the −30 kV, and the 1° rotation nearly always causes at least a 1 m position change, which removes the lower lobe. It is still the case that electrostatics at $K_P = 2-$ are less significant than 0.0001° of attitude uncertainty, at $K_P = 8$ including electrostatics is roughly equivalent to 0.001° of attitude uncertainty, the worst case is more significant than 1° of uncertainty, and that including eddy torques is similar to 1° of uncertainty. The maximum position difference is observed for the worst-case −30 kV and is 5.77 km.

It is interesting to look at how the spread from including or neglecting a certain perturbation or attitude uncertainty changes with time. To do this, the 95% upper bound is found for each perturbation/attitude uncertainty at each time in Figure 8d. This is done by sorting the Δr and taking the 475th element since there are 500 entries. This gives an empirical estimate to the 2σ covariance bound that should be associated with the initial attitude uncertainty or the unmodeled perturbations. This covariance bound is plotted in Figure 8 for all the perturbations and the limiting attitude uncertainties of 1° and 0.0001°.

The worst-case constant voltage of −30 kV causes the largest covariance, followed by the 1° attitude uncertainty, then eddy torques, then $K_P = 8$, then $K_P = 2-$, and the 0.0001° attitude uncertainty which are similar. All of the perturbations/attitude uncertainties lead to between 0.5 and 2 km covariance after 3 h and seem to be accelerating. In the case of a solar storm at $K_P = 8$, the covariance bounds do not need to be drastically changed from the normal ones associated with attitude uncertainty. However, if the worst-case charging is maintained, the covariance bounds need to be expanded beyond their normal values. Eddy torques, which act no matter what K_P is, always cause large covariances.

7. Conclusions

The dynamical motion prediction of a charged HAMR plate with center of pressure offset from center of mass is a very sensitive problem. Without very precise knowledge of all torques on it, and a very precise measurement of the initial attitude, it is difficult to model its motion accurately—including or neglecting these effects can lead to 5.77 km displacements after only 3 h. It is found that at $K_P = 2-$, electrostatics are less important than 0.0001° of attitude uncertainty, at $K_P = 8$ it is about the same as 0.001°, a constant voltage of −30 kV is more significant than 1°, and eddy torques are about equal to 1° of uncertainty. Additionally, the covariance bounds for neglecting these perturbations or attitude uncertainty are between 200 m and 900 m after only 2 h, and between 0.5 and 2 km after 3 h.

This shows that (1) HAMR objects with highly attitude-dependent area-to-mass ratios are very sensitive. Any unmodeled disturbances or initial attitude uncertainty can lead to 5 km departures after only a few hours. (2) Even in a relatively benign ($K_P = 2-$) charging environment, the covariance bounds for such objects ought to be enlarged significantly to account for eddy torques in order to track them accurately. (3) If an object charges to a very negative voltage and holds that voltage, the covariance bounds need to be enlarged to account for this unmodeled disturbance. Although the electromagnetic perturbations considered here do not change the orbits in predictable ways because of the attitude and Solar Radiation Pressure coupling, they do change the orbits significantly. Accounting for such perturbations in the form of inflating the covariance is important for tracking such objects.

Acknowledgments
The CCMC website which holds the parameters used for the Tsganenko model is http://ccmc.gsfc.nasa.gov/requests/instant/tsyganenko.php. The empirical model for environmental fluxes Denton et al. (2015) can be found at http://gemelli.spacescience.org/mdenton/. This work is sponsored by the Air Force Office of Scientific Research by grant FA9550-15-1-0407.

References

Balcon, N., Payan, D., Belhaj, M., Tondu, T., & Inguimbert, V. (2012). Secondary electron emission on space materials: Evaluation of the total secondary electron yield from surface potential measurements. *IEEE Transactions on Plasma Science*, *40*(2), 282–290.

Bhavnani, K. H., & Vancour, R. (1991). Coordinate systems for space and geophysical applications (Tech. Rep.). Phillips Laboratory, Air Force Systems Command.

Chen, N. M. A. (1975). Isolated cold plasma regions: Observations and their relation to possible production mechanisms. *Journal of Geophysical Research*, *80*(7), 1009–1013.

Davis, V., Gardner, B., Mandell, M., & Wilcox, K. (2011). *NASCAP-2k user's manual* (4.1 ed.). San Diego, CA: Science Applications International Corporation.

Davis, V., & Mandell, M. J. (2011). *Plasma interactions with spacecraft. Volume 2, NASCAP-2 K scientific documentation for version 4.1* (4.1 ed.). Science Applications International Corp.

Denton, M., Thompsen, M., Jordanova, V., Henderson, M., Borovsky, J., Denton, J., et al. (2015). An empirical model of electron and ion fluxes derived from observations at geosynchronous orbit. *AGU Space Weather*, *13*, 233–249.

Dever, J. A., de Groh, K. K., Townsend, J. A., & Townsend, J. A. (1998). *Mechanical properties degradation of teflon FEP returned from the Hubble Space Telescope*. Washington, DC: American Institute of Aeronautics and Astronautics.

Fennell, J. F., Koons, H. C., Leung, M., & Mizera, P. (1983). *A review of SCATHA satellite results: Charging and discharging* (pp. 3–11). Noordwijk, NL: European Space Agency.

Ferguson, D., Hoffmann, R., Cooper, R., & Hughes, J. (2017). 1997–2002 Solar array string failures revisited. *Journal of Spacecraft and Rockets*, *54*(3), 542–553.

Finckenor, M. (1999). Multilayer insulation material guidelines (Tech. Rep.). NASA Marshall Space Flight Center.

Früh, C., Ferguson, D., Lin, C., & Jah, M. (2014). The effect of passive electrostatic charging on near-geosynchronous high area-to-mass ratio objects. In *Proc. AAS Space Flight Mechanics Meeting*, Santa Fe, NM.

Gibson, W. C. (2007). *The method of moments in electromagnetics*. Bora Raton: Chapman & Hall.

Griffiths, D. J. (1999). *Introduction to electrodynamics* (3rd ed.). Upper Saddle River, NJ: Prentice Hall.

Hughes, J., & Schaub, H. (2016). Charged geosynchronous debris perturbation using rapid electromagnetic force and torque evaluation. In *Advanced Maui Optical and Space Surveillance Technologies Conference*, Wailea, Maui, Hawaii.

Hughes, J., & Schaub, H. (2017a). Rapid charged geosynchronous debris perturbation modeling of electromagnetic disturbances. In *AAS Spaceflight Mechanics Meeting*, San Antonio, TX.

Hughes, J., & Schaub, H. (2017b). Spacecraft electrostatic force and torque expansions yielding appropriate fidelity measures. In *AAS Spaceflight Mechanics Meeting*, San Antonio, TX.

Korth, H., Thomsen, M. F., Borovsky, J. E., & McComas, D. J. (1999). Plasma sheet access to geosynchronous orbit. *Journal of Geophysical Research*, *104*(A11), 25,047—25,062. https://doi.org/10.1029/1999JA900292

Lai, S. T. (2011). *Fundamentals of spacecraft charging: Spacecraft interactions with space plasmas*. Princeton, NJ: Princeton University Press.

Lin, Y., & Joy, D. C. (2005). A new examination of secondary electron yield data. *Surface and Interface Analysis*, *57*, 895–900.

Mullen, E. G., Gussenhoven, M. S., Hardy, D. A., Aggson, T. A., & Ledley, B. G. (1986). Scatha survey of high-voltage spacecraft charging in sunlight. *Journal of Geophysical Research*, *91*(A2), 1474–1490. https://doi.org/10.1029/JA091iA02p01474

Ortiz Gomez, N., & Walker, S. J. I. (2015). Eddy currents applied to de-tumbling of space debris: Feasibility analysis, design and optimization aspects. *Acta Astronautica*, *114*, 34–53.

Paul, S. N., & Früh, C. (2017). Space debris charging and its effect on orbit evolution. *Journal of Guidance, Control, and Dynamics*, *0*, 1–19.

Schaub, H., & Junkins, J. L. (2009). *Analytical mechanics of space systems* (2nd ed.). AIAA Education Series, Reston, VA.

Schildknecht, T., Musci, R., Frueh, C., & Ploner, M. (2008). Color photometry and light curve observations of space debris in geo. In *Procedings of the Internaitonal Astronautical Congress*, Wailea, Maui, Hawaii.

Schildknecht, T., Muscia, R., Plonera, M., Beutlera, G., Fluryb, W., Kuuselac, J., et al. (2004). Optical observations of space debris in geo and in highly-eccentric orbits. *Advances in Space Research*, *34*(5), 901–911.

Stern, D. P. (1975). The motion of a proton in the equatorial magnetosphere. *Journal of Geophysical Research*, *90*(4), 595–599.

Stevenson, D., & Schaub, H. (2013). Optimization of sphere population for electrostatic multi sphere model. *IEEE Transactions on Plasma Science*, *41*(12), 3526–3535.

Tsyganenko, N. A. (1989). A magnetospheric magnetic field model with a warped tail current sheet. *Planetary and Space Science*, *37*, 5–20.

Volland, H. (1973). A semiemperical model of large-scale magnetospheric electric fields. *Journal of Geophysical Research*, *78*(1), 171–180.

Wie, B. (2008). *Space vehicle dynamics and control* (2nd ed.). AIAA Education Series, Reston, VA.

Wiesel, W. E. (2016). Estimating nongravitational accelerations on high area to mass ratio objects. *Journal of Guidance, Control, and Dynamics*, *39*(6), 1438–1443. https://doi.org/10.2514/1.G001464